Physics of Fluids

RESEARCH ARTICLE | MARCH 17 2025

Anomalous water slippage in pulsatile microfluidics caused by nanoscale emergent viscoelasticity

Special Collection: Multi-Scale, Multi-Media and Multi-Physics Rheology

Ulises Torres-Herrera

Physics of Fluids 37, 032031 (2025)
https://doi.org/10.1063/5.0256422

Articles You May Be Interested In

Permeability and effective slip in confined flows transverse to wall slippage patterns

Physics of Fluids (August 2016)

Dynamic permeability of fluids in rectangular and square microchannels: Shift and coupling of viscoelastic bidimensional resonances

Physics of Fluids (January 2021)

Dispersion due to electroosmotic flow in a circular microchannel with slowly varying wall potential and hydrodynamic slippage

Physics of Fluids (November 2012)

AIP Publishing

Physics of Fluids ARTICLE pubs.aip.org/aip/pof

Anomalous water slippage in pulsatile microfluidics caused by nanoscale emergent viscoelasticity

Cite as: Phys. Fluids **37**, 032031 (2025); doi: 10.1063/5.0256422
Submitted: 4 January 2025 · Accepted: 15 February 2025 ·
Published Online: 17 March 2025

Ulises Torres-Herrera[1,2,a)]

AFFILIATIONS

[1]Department of Civil and Environmental Engineering, The Hong Kong Polytechnic University, Hung Hom, Kowloon 999077, Hong Kong SAR, People's Republic of China
[2]Facultad de Química, Universidad Autónoma del Estado de México, Toluca de Lerdo 50120, Mexico

Note: This paper is part of the Special Topic, Multi-Scale, Multi-Media and Multi-Physics Rheology.

[a)]**Author to whom correspondence should be addressed:** torres.herrera.ulises@hotmail.com

ABSTRACT

A theoretical model is proposed to study fluid dynamics in microchannels under pulsatile external forcing. This model incorporates the fluid/wall interaction considering that a rough interface consists of an array of parallel nanometric channels coupled with the bulk flow generated in the main microfluidic channel. Consequently, a theoretical technique is developed to compute an exact analytical solution. This solution is fundamental for the study of the multiscale flow dynamics involved in the interaction between adjacent flows with confining dimensions and properties that differ by orders of magnitude. This is particularly relevant for the case of confined water, as recent evidence suggests a confinement-dependent viscoelastic behavior. Under these conditions, considerable flow slippage is predicted at the interface between nano-confined water and larger confinements. This finding is understood in terms of the propagation of elastic waves that are generated in the nanometric channels and propagated and magnified in the microchannel. Finally, the stability and robustness of the solution for all ranges of channel dimensions and relaxation times is exploited to carry out a comprehensive exploration of the key physical conditions that determine the arising and persistence of anomalous flow slippage due to size-dependent viscoelasticity. The results of this model are of interest for a better understanding of the impact of fluid/wall interactions in dynamic situations, as for a reassessment of typical assumptions of no-slippage at the fluid/wall interface, widely employed in microfluidics of high-polarity channels.

I. INTRODUCTION

With the development of micro and nanofluidics, a new era in flow systems has emerged. The constantly increasing control of flow conditions and dimensions at micrometer and submicrometer scales allows novel devices to incorporate multiple substations into a single chip (Neužil *et al.*, 2012; Tomita *et al.*, 2024), with the capability to address complex physical and chemical problems in a very small, low-supply consumption and low-waste generation system (Ochoa *et al.*, 2023; Islam *et al.*, 2024; Kenari *et al.*, 2022; and Dou *et al.*, 2024).

Along with technological progress, new physical phenomena have been encountered in the study of fluids subjected to small confinements. Fluid dynamics is still governed by the same conservation equations that rule their macroscopic behavior, even at sizes of the order of a few thousands of fluid molecules (Thomas and McGaughey, 2009; Jin and Ren, 2024); nevertheless, new forces and effects arise in nanometric confinements, leading to emerging phenomena that do not have an equivalence in macroscopic flows (Corral-Casas *et al.*, 2024; Torres-Herrera and Corvera Poiré, 2021; Torres-Herrera, 2022; Shang *et al.*, 2017; Si *et al.*, 2023; and Squires and Quake, 2005).

One of the most remarkable emerging properties is the viscoelasticity of nanoconfined fluids that are typically regarded Newtonian in macroscopic rheological tests (Yuan *et al.*, 2020). To understand such findings, experimental and theoretical work has shed light onto the formation of long-time hydrogen bonds and intermolecular networks that present a global elastic response to pulsatile external forcing in nanometric confinements. From an experimental point of view, the elastic component in the rheological response of water was detected with high-frequency oscillating shear rates exerted on water nanodroplets with atomic force microscopy; in particular, a size-dependent relaxation time of water on the order of 10^{-5} s was encountered for plates with separation between 2 and 5 nm (Kapoor *et al.*, 2014). From a theoretical and computational point of view, the formation of these molecular aggregates depends strongly on the interaction between water molecules and also between water and the polar sites of the solid substrate and the ones of the probe employed in the nano-rheological tests. However, the dynamic properties of nanoconfined fluids have not been completely explored, especially when they are integrated into larger flow systems, such as microfluidic devices.

The study of flow systems across macroscopic, mesoscopic, and nanoscopic dimensions is an emerging area that has been explored by many theoretical, computational, and experimental approaches. In this regard, some theoretical studies have addressed the simulation of complex flow systems across multiple scales using a hybrid atomistic/continuum approach (Borg *et al.*, 2013). These simulations combine molecular dynamics and computational fluid dynamics and have been very successful in studying the role of chemical forces and interactions at the nanoscale, for their subsequent incorporation in the dynamics of micrometric and submicrometric flow systems. However, their theoretical predictions are usually limited to short simulation times, because of their high computational cost (Mohamed and Mohamad, 2010). Moreover, the physical consistency of hybrid simulations is always challenging, since the definition of the interface between the two modeled scales is very hard to define in simple terms, from a conceptual and a practical/computational point of view. This is particularly important in hybrid simulations because both levels of theory, atomistic and continuum, rely on different descriptors to track down the dynamics of the system. In consequence, the translation between both levels of description is always an arduous task and has been faced by different approaches in the literature (Borg *et al.*, 2013; Alexeev *et al.*, 2020).

Given the conceptual challenges that hybrid methods face, alternative theoretical approaches have been developed to adapt and extend the models of continuum mechanics for very small scales of confinement. To do so, it is necessary to incorporate peculiarities of the nanoscale, such as anomalous intermolecular forces, fluctuation of thermodynamic properties, interfacial phenomena, and thermal vibration. The accurate modeling of those multiscale effects is a work in progress that involves the incorporation of nonconventional effective boundary conditions, additional terms/forces in the equations of motion of continuum mechanics, or even effective constitutive relations that account for micro- and nano-rheology integrated with interfacial forces (Sagis and Öttinger, 2013; Öttinger and Venerus, 2014; and Vazquez-Vergara *et al.*, 2021a). In some cases, these effective models allow for an analytical solution that unveils the persistence of nanoscale forces at larger scales, dictating the dynamics of complex fluids in microfluidic devices (Vazquez-Vergara *et al.*, 2021b; Stoecklein and Di Carlo, 2019).

Among the theoretical predictions and computational simulations obtained by continuum models, the analytical results show several interesting features. For instance, some analytical solutions are valid and mathematically convergent in a wide range of time scales and system sizes, unlike the solutions obtained by numerical methods. This is of relevance when dealing with dynamic systems where many spatial scales are coupled, since the net response of these systems requires an accurate solution at all scales simultaneously (Weinan, 2011; Chashechkin, 2016; and Turkyilmazoglu, 2020). A second feature of analytical results is their clarity. By inspection of the mathematical expressions, it is possible to analyze and determine the role of each driving force involved in the response of a dynamic system. A deeper study could even show that some of these physical parameters are combined into effective parameters, understood as global mechanisms that compete or magnify each other (Vazquez-Vergara *et al.*, 2021b; Collepardo-Guevara and Poiré, 2007). Another feature of interest from a computational point of view arises when analytical expressions are implemented in optimization applications, allowing for fast and reliable computation of derivatives of the response of a system, as a function of each design parameter. In this manner, analytical gradient data widen the range of possible optimization methods employed.

In the particular case of microfluidic systems, analytical studies have accurately predicted the arising of resonances in pulsatile flows. This magnified response of the system at specific pulsation frequencies is caused by the interaction of several elastic forces, whose competition is especially relevant at micrometric scales, such as channel elasticity, bending vibration, fluid viscoelasticity, and surface tension (Torres-Herrera, 2021; Corvera Poiré and Hernández-Machado, 2010; Hagsäter *et al.*, 2007; and Vazquez-Vergara *et al.*, 2021a). Nevertheless, a current challenge in microfluidics and nanofluidics is the prediction of resonances in complex flow systems where the macro-, meso-, and nanoscales are integrated.

There are many realizations of flow systems with channels of sizes that span over several scales, whether fractal flow networks (Liu *et al.*, 2015; 2016; Torres-Herrera and Nakamura, 2022), biological vascular systems (Soltani and Chen, 2013; Alastruey *et al.*, 2016), or channels with complex cross-sectional geometry or with micro and nano-patterned channels (Priest, 2010; Gerónimo *et al.*, 2022). In particular, the role of rugosity as a nanometric confinement is a topic of recent development Zampogna *et al.* (2019) and Bolaños and Vernescu (2017). Moreover, its coupling to the complex rheology or interfacial forces present in microfluidic systems is pending to be explored under pulsatile conditions.

In this work, a model of a rectangular microchannel conveying pulsatile water flow is proposed. One of its walls exhibits a pattern of nanometric parallel cavities that resemble, to some extent, a simplified version of rugosity. The dimensions of such cavities are such that the nanoscale-emergent viscoelasticity encountered by Kapoor *et al.* (2014) is incorporated into the model. Then, the derivation of an analytical solution is carried out, followed by a thorough analysis of its main features and consequences. In particular, viscoelasticity in nanometric cavities produces an increase in flow velocity at the interface with the main channel. These findings are understood in terms of an effective slip length.

II. MODEL

The system of study consists of a rectangular microfluidic channel. Of the four walls that delimit the channel, three are considered rugosity-free surfaces. The last surface exhibits a rugosity consisting of parallel equidistant rectangular subchannels with a given width and height that lie in the nanoscale (see Fig. 1).

In order to model in full detail the complex fluid dynamics developed in the proximity of the rough interface, the system is split into several regions. The first region is the one where the main flow occurs, that is regarded as a flow surrounded by three conventional walls with no-slip boundary conditions, while the last wall is modeled as a complex surface where the main stream is in contact with multiple small subchannels. Then, the flow at the rough interface is modeled as a set of subchannels, each one consisting of three walls, namely, the ones produced by each rugosity, and a fourth surface, open and in contact with the bulk stream. Each subchannel develops a time-dependent fluid dynamics in the proximity of the small cavity created by each peak of roughness of the material, so the fluid within each subchannel is surrounded by three small walls produced by roughness of the material, while the fourth surface is in contact with the main flow.

The most important achievement of this model is that it allows one to consider the singular dynamics produced by the anomalous interaction of the walls and water molecules under nanoconfinement. In particular, all subchannels exhibit a rheological dynamics given by a size-dependent viscoelastic relaxation time, while the bulk channel exhibits a conventional Newtonian behavior. The mathematical considerations of the model are detailed in Subsections II A–II D. The system of study is summarized in Fig. 1.

A. Modeling the bulk flow

A uniaxial flow across a main rectangular microchannel is produced by a pressure gradient of arbitrary time dependence. Such a driving force is independent of the spatial coordinates, as a consequence of the constant cross-sectional area of the channel and rigid walls that imply that the pressure gradient is propagated instantly from the pressure source toward the rest of the channel. In such conditions, the equation of motion for the bulk phase is given by

$$\rho \frac{\partial v_I}{\partial t} = -\frac{\partial p}{\partial z} + \mu\left(\frac{\partial^2 v_I}{\partial x^2} + \frac{\partial^2 v_I}{\partial y^2}\right) \quad \text{for } 0 \le x \le W_I, \quad -\frac{H_I}{2} \le y \le \frac{H_I}{2}, \tag{1}$$

where $v_I(x, y, t)$ is the flow velocity in the bulk phase along the z direction, μ is the dynamic viscosity, and ρ is the fluid density.

Afterward, Eq. (1) is rewritten in terms of dimensionless parameters, as

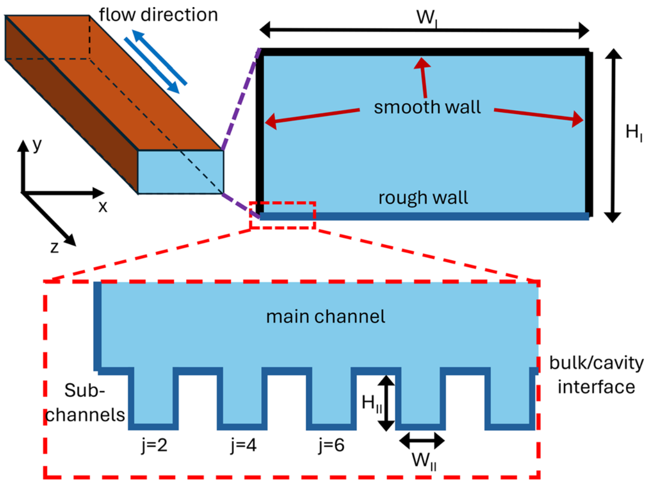

FIG. 1. Description of the system of study. The microchannel is made by four walls, three smooth and one with a pattern of perfect rectangular subchannels. Notation of numeration of subchannels and channel dimensions is detailed.

$$\frac{\partial \tilde{v}_I}{\partial \tilde{t}} = 2\frac{\frac{\partial p}{\partial z}}{\left(\frac{\partial p}{\partial z}\right)_0} + \frac{1}{4}\left(\frac{\partial^2 \tilde{v}_I}{\partial \tilde{x}^2} + \chi^2 \frac{\partial^2 \tilde{v}_I}{\partial \tilde{y}^2}\right) \quad \text{for } 0 \le \tilde{x} \le 1, \quad -\frac{1}{2} \le \tilde{y} \le \frac{1}{2}, \tag{2}$$

where the following parameters are defined:

$$\tilde{v}_I \equiv \frac{v_I}{-\frac{W_I^2}{8\mu}\left(\frac{\partial p}{\partial z}\right)_0}, \quad \tilde{x} \equiv \frac{x}{W_I}, \quad \tilde{y} \equiv \frac{y}{H_I}, \quad \tilde{t} \equiv \omega_\mu t, \quad \omega_\mu \equiv \frac{4\mu}{\rho W_I^2}, \quad \chi \equiv \frac{W_I}{H_I}, \tag{3}$$

where the characteristic amplitude of pressure gradient along flow direction has been defined as

$$\left(\frac{\partial p}{\partial z}\right)_0 \equiv -\mathrm{Max}\left(\frac{|p_{out}(t) - p_{in}(t)|}{L}\right), \tag{4}$$

where p_{in} and p_{out} are the pressure at the inlet and outlet of the microchannel, whereas L is the microchannel length.

Then, the Fourier transform of Eq. (2) is carried out, as follows:

$$-i\tilde{\omega}\hat{v}_I = 2\frac{\frac{\partial \hat{p}}{\partial z}}{\left(\frac{\partial p}{\partial z}\right)_0} + \frac{1}{4}\left(\frac{\partial^2 \hat{v}_I}{\partial \tilde{x}^2} + \chi^2 \frac{\partial^2 \hat{v}_I}{\partial \tilde{y}^2}\right), \tag{5}$$

where $\hat{v}_I$ stands for the Fourier transform of $\tilde{v}_I$.

B. Modeling the flow in rugosity-induced nano-cavities

The flow developing in the vicinity of the rough interface is modeled here as a sequence of small rectangular cavities coupled to the main channel. Flow across each cavity is governed by the unsteady Stokes equation of unidirectional flow, in an analogous manner to the treatment developed for the unidirectional flow across the main channel. Nevertheless, the rheological properties of water inside of nanometric confinements are incorporated in the flow within the cavities by considering a single Maxwellian relaxation time that characterizes the rheological behavior of nanoconfined water. In particular, the relaxation time is chosen to be on the same order of magnitude as the one measured experimentally by Kapoor *et al.* (2014). Within the framework of Maxwellian fluids, the operator $1 + t_r \frac{\partial}{\partial t}$ is understood as an elastic term that is added to the viscous Newtonian term, and accounts for the formation of water structures. With these considerations, the flow inside each cavity is governed by the following differential equation:

$$\rho \frac{\partial v_{II,j}}{\partial t} + \rho t_r \frac{\partial^2 v_{II,j}}{\partial t^2} = -\frac{\partial p}{\partial z} - t_r \frac{\partial}{\partial t}\left(\frac{\partial p}{\partial z}\right) + \mu\left(\frac{\partial^2 v_{II,j}}{\partial x^2} + \frac{\partial^2 v_{II,j}}{\partial y^2}\right)$$
$$\text{for } j = 2, 4, \ldots, 2N, \quad x_{ini,j} \le x \le x_{fin,j}, \quad -\frac{H_{II}}{2} \le y \le \frac{H_{II}}{2}, \tag{6}$$

where $v_{II,j}(x, y, t)$ is the z-component of the flow velocity in the jth cavity, each cavity is located between $x = x_{ini,j}$ and $x_{fin,j}$, defined as

$$x_{ini,j} = \frac{(j-1)W_I}{2N+1}, \quad x_{fin,j} = \frac{jW_I}{2N+1}, \tag{7}$$

and t_r is the viscoelastic relaxation time that characterizes the rheological response of water under nanoconfinement (Kapoor *et al.*, 2014). Then, the equations of motion given by Eq. (6) are rewritten in terms of dimensionless parameters, leading to

$$\frac{\partial \tilde v_{II,j}}{\partial \tilde t}+\tilde t_r\frac{\partial^2 \tilde v_{II,j}}{\partial \tilde t^2}=2\frac{\frac{\partial p}{\partial z}}{\left(\frac{\partial p}{\partial z}\right)_0}+2\tilde t_r\frac{\frac{\partial}{\partial \tilde t}\left(\frac{\partial p}{\partial z}\right)}{\left(\frac{\partial p}{\partial z}\right)_0}+\frac{1}{4}\left(\frac{\partial^2 \tilde v_{II,j}}{\partial \tilde x^2}+\chi^2\frac{\partial^2 \tilde v_{II,j}}{\partial \tilde y^2}\right)$$
$$\text{for } j=2,4,\ldots,2N,\quad \tilde x_{ini,j}\le\tilde x\le\tilde x_{fin,j},\quad -\frac{1}{2f}\le\tilde y\le\frac{1}{2f}, \tag{8}$$

where the following parameters are defined:

$$\tilde v_{II,j}\equiv\frac{v_{II,j}}{-\frac{W_I^2}{8\mu}\left(\frac{\partial p}{\partial z}\right)_0},\qquad \tilde t_r\equiv\omega_\mu t_r,\qquad f\equiv\frac{H_I}{H_{II}},$$
$$\tilde x_{ini,j}\equiv\frac{x_{ini,j}}{W_I},\qquad \tilde x_{fin,j}\equiv\frac{x_{fin,j}}{W_I}, \tag{9}$$

and the Fourier transform of Eq. (8) is carried out as follows:

$$-i\tilde\omega(1-i\tilde\omega\tilde t_r)\hat v_{II,j}=2(1-i\tilde\omega\tilde t_r)\frac{\frac{\partial\hat p}{\partial z}}{\left(\frac{\partial p}{\partial z}\right)_0}+\frac{1}{4}\left(\frac{\partial^2\hat v_{II,j}}{\partial\tilde x^2}+\chi^2\frac{\partial^2\hat v_{II,j}}{\partial\tilde y^2}\right), \tag{10}$$

where $\hat v_{II,j}$ stands for the Fourier transform of $\tilde v_{II,j}$.

C. Modeling no slip boundary conditions

In order to solve Eqs. (5) and (10), boundary conditions are incorporated to account for the interaction between the fluid and the channel walls. In all cases considered, the fluid does not slip near the fluid/wall interface. First, the no-slip boundary condition is presented for the three smooth walls that surround the main channel. For the side walls, this is given by

$$\hat v_I(\tilde x=0,\tilde y,\tilde\omega)=0\quad\text{and}\quad\hat v_I(\tilde x=1,\tilde y,\tilde\omega)=0, \tag{11}$$

while the boundary condition at upper wall is given by

$$\hat v_I\left(\tilde x,\tilde y=\frac{1}{2},\tilde\omega\right)=0. \tag{12}$$

In addition, each subchannel j also exhibits three smooth walls (notice that the cavities are located at even values of j in Fig. 1). Thus, no-slip boundary condition is given by

$$\hat v_{II,j}\left(\tilde x=\tilde x_{ini,j},\tilde y,\tilde\omega\right)=0\quad\text{and}\quad\hat v_{II,j}\left(\tilde x{=}_{fin,j},\tilde y,\tilde\omega\right)=0,$$
$$\text{for}\quad j=2,4,\ldots,2N, \tag{13}$$

while the boundary condition at bottom wall is given by

$$\hat v_{II,j}\left(\tilde x,\tilde y=-\frac{1}{2f},\tilde\omega\right)=0,\quad\text{for}\quad j=2,4,\ldots,2N. \tag{14}$$

D. Coupling bulk and interfacial flows

In order to couple the fluid dynamics at the main channel and the subchannels, it is considered that the interface between the bulk water phase in main microchannel and each nano-confined water phase in the subchannels is ruled by continuity of flow velocity and by continuity of shear stress. These relations are given as follows:

$$\hat v_I\left(\tilde x,\tilde y=-\frac{1}{2},\tilde\omega\right)=\begin{cases}\hat v_{II,j}\left(\tilde x,\tilde y=\frac{1}{2f},\tilde\omega\right), & \text{if } \tilde x_{ini,j}\le\tilde x\le\tilde x_{fin,j}\quad\text{for } j\text{ even},\\ 0, & \text{if } \tilde x_{ini,j}\le\tilde x\le\tilde x_{fin,j}\quad\text{for } j\text{ odd},\end{cases} \tag{15}$$

$$-\frac{\partial\hat v_I}{\partial\tilde y}\left(\tilde x,\tilde y=-\frac{1}{2},\tilde\omega\right)=-\frac{1}{1-i\tilde\omega\tilde t_r}\frac{\partial\hat v_{II,j}}{\partial\tilde y}\left(\tilde x,\tilde y=\frac{1}{2f},\tilde\omega\right),$$
$$\text{if } \tilde x_{ini,j}\le\tilde x\le\tilde x_{fin,j}\quad\text{for } j\text{ even}. \tag{16}$$

Notice that the condition of continuity of stress tensor is only defined in the region where two fluid phases are in contact, i.e., for even values of j in Eq. (16); this condition is not needed in the points where bulk flow is directly in contact with the wall without a subchannel, since in such case, the no-slip boundary condition, as shown in Eq. (15) for odd values of j, is sufficient to compute the solution.

III. ANALYTICAL SOLUTION

The analytical solution is carried out in two stages. In the first stage, a general solution is found for each of the flow channels, namely, a solution for the main channel and for each subchannel labeled as $j=2,4,\ldots,2N$. In the second stage, the mathematical details to compute the coefficients of each channel are given, in order to compute the complete solution of this system in an analytical and exact mean in the form of a series solution, as

$$\hat v_I(\tilde x,\tilde y,\tilde\omega)=\sum_{n=1}^{\infty}\tilde C_{I,n}(\tilde y,\tilde\omega)\sin n\pi\tilde x, \tag{17}$$

that is substituted in Eq. (5), leading to the following differential equation for the spatially dependent coefficients $\tilde C_{I,n}(\tilde x,\tilde y,\tilde\omega)$, as follows:

$$\sum_{n=1}^{\infty}\left(\chi^2\frac{d^2\tilde C_{I,n}}{d\tilde y^2}-n^2\pi^2\tilde C_{I,n}+4i\tilde\omega\tilde C_{I,n}+16\left(\frac{1-(-1)^n}{n\pi}\right)\left(\frac{\frac{\partial\hat p}{\partial z}}{\left(\frac{\partial p}{\partial z}\right)_0}\right)\right)$$
$$\times\sin n\pi\tilde x=0. \tag{18}$$

Solution of Eq. (18) is carried out for each nth mode separately, leading to the following general solution:

$$\tilde C_{I,n}=-\left(\frac{\frac{\partial p}{\partial z}}{\left(\frac{\partial p}{\partial z}\right)_0}\right)\left(\frac{16\left(1-(-1)^n\right)}{n\pi(-n^2\pi^2+4i\tilde\omega)}\right)$$
$$+c_{1,n}\cos\left(\frac{\tilde y}{\chi}\sqrt{-n^2\pi^2+4i\tilde\omega}\right)+c_{2,n}\sin\left(\frac{\tilde y}{\chi}\sqrt{-n^2\pi^2+4i\tilde\omega}\right),$$
$$\text{for}\quad n=1,2,\ldots, \tag{19}$$

where the coefficients $c_{1,n}$ and $c_{2,n}$ will be computed in Sec. III A.

Afterward, a solution is proposed for each subchannel, of the form

$$\hat{v}_{II,j}(\tilde{x},\tilde{y},\tilde{\omega}) = \sum_{n=1}^{\infty} \tilde{C}_{II,j,n}(\tilde{y},\tilde{\omega}) \sin(n\pi(2N+1)(\tilde{x}-\tilde{x}_{ini,j})), \tag{20}$$

which, after substitution in Eq. (10), leads to the following differential equation for the spatially dependent coefficients $\tilde{C}_{II,j,n}(\tilde{y},\tilde{\omega})$:

$$\sum_{n=1}^{\infty}\left(\chi^2\frac{d^2\tilde{C}_{II,j,n}}{d\tilde{y}^2} - n^2\pi^2(2N+1)^2\tilde{C}_{II,j,n} + 4i\tilde{\omega}(1-i\tilde{\omega}\tilde{t}_r)\tilde{C}_{II,j,n} + 16(1-i\tilde{\omega}\tilde{t}_r)\left(\frac{1-(-1)^n}{n\pi}\right)\left(\frac{\dfrac{\partial\hat{p}}{\partial z}}{\left(\dfrac{\partial p}{\partial z}\right)_0}\right)\right)$$
$$\times\ \sin(n\pi(2N+1)(\tilde{x}-\tilde{x}_{ini,j})) = 0, \quad \text{for } j = 2,4,\ldots,2N. \tag{21}$$

The solution of Eq. (21) is carried out for each nth mode and for each jth subchannel separately, given by

$$\tilde{C}_{II,j,n} = -\left(\frac{\dfrac{\partial p}{\partial z}}{\left(\dfrac{\partial p}{\partial z}\right)_0}\right)\left(\frac{16(1-(-1)^n)(1-i\tilde{\omega}\tilde{t}_r)}{n\pi(-n^2\pi^2(2N+1)^2+4i\tilde{\omega}(1-i\tilde{\omega}\tilde{t}_r))}\right) + c_{3,j,n}\cos\left(\frac{\tilde{y}}{\chi}\sqrt{-n^2\pi^2(2N+1)^2+4i\tilde{\omega}(1-i\tilde{\omega}\tilde{t}_r)}\right)$$
$$+\, c_{4,j,n}\sin\left(\frac{\tilde{y}}{\chi}\sqrt{-n^2\pi^2(2N+1)^2+4i\tilde{\omega}(1-i\tilde{\omega}\tilde{t}_r)}\right), \quad \text{for } n = 1,2,3,\ldots \quad \text{and} \quad j = 2,4,\ldots,2N, \tag{22}$$

where the coefficients $c_{3,j,n}$ and $c_{4,j,n}$ will be computed in Sec. III A.

It is important to emphasize that the solution proposed in Eqs. (17) and (20) is consistent with the no-slip boundary conditions at the side walls as defined in Eqs. (11) and (13). However, it is still necessary to consider the boundary conditions at the top wall of the main channel and at the bottom wall of each subchannel, given by Eqs. (12) and (14). For the main channel, this is given by

$$\tilde{C}_{I,n}\left(\tilde{y}=\frac{1}{2},\tilde{\omega}\right) = 0, \quad \text{for } n = 1,2,3,\ldots, \tag{23}$$

which, after substitution in Eq. (17), leads to the following expression:

$$-\left(\frac{\dfrac{\partial p}{\partial z}}{\left(\dfrac{\partial p}{\partial z}\right)_0}\right)\left(\frac{16(1-(-1)^n)}{n\pi(-n^2\pi^2+4i\tilde{\omega})}\right) + c_{1,n}\cos\left(\frac{1}{2\chi}\sqrt{-n^2\pi^2+4i\tilde{\omega}}\right) + c_{2,n}\sin\left(\frac{1}{2\chi}\sqrt{-n^2\pi^2+4i\tilde{\omega}}\right) = 0,$$
$$\text{for } n = 1,2,3,\ldots. \tag{24}$$

On the other hand, each subchannel requires a similar boundary condition for the bottom wall as follows:

$$\tilde{C}_{II,j,n}\left(\tilde{x},\tilde{y}=-\frac{1}{2f},\tilde{\omega}\right) = 0, \quad \text{for } n = 1,2,3,\ldots \quad \text{and} \quad j = 2,4,\ldots,2N, \tag{25}$$

and, after substitution in Eq. (20), the following expression is obtained:

$$-\left(\frac{\dfrac{\partial p}{\partial z}}{\left(\dfrac{\partial p}{\partial z}\right)_0}\right)\left(\frac{16(1-(-1)^n)(1-i\tilde{\omega}\tilde{t}_r)}{n\pi(-n^2\pi^2(2N+1)^2+4i\tilde{\omega}(1-i\tilde{\omega}\tilde{t}_r))}\right) + c_{3,j,n}\cos\left(\left(-\frac{1}{2f}\right)\frac{1}{\chi}\sqrt{-n^2\pi^2(2N+1)^2+4i\tilde{\omega}(1-i\tilde{\omega}\tilde{t}_r)}\right)$$
$$+\, c_{4,j,n}\sin\left(\left(-\frac{1}{2f}\right)\frac{1}{\chi}\sqrt{-n^2\pi^2(2N+1)^2+4i\tilde{\omega}(1-i\tilde{\omega}\tilde{t}_r)}\right) = 0, \quad \text{for } n = 1,2,3,\ldots \text{ and } j = 2,4,\ldots,2N. \tag{26}$$

Finally, it is necessary to consider the coupling that occurs at the interface between the flow in the main channel and each of the subchannels. This coupling is given by the continuity of flow velocity and by the continuity of shear stress. First, the condition of continuity of flow velocity leads to

$$\begin{aligned}&\sum_{n=1}^{\infty}\left(-\left(\frac{\dfrac{\partial p}{\partial z}}{\left(\dfrac{\partial p}{\partial z}\right)_0}\right)\left(\frac{16(1-(-1)^n)}{n\pi(-n^2\pi^2+4i\tilde{\omega})}\right)+c_{1,n}\cos\left(-\frac{1}{2\chi}\sqrt{-n^2\pi^2+4i\tilde{\omega}}\right)+c_{2,n}\sin\left(-\frac{1}{2\chi}\sqrt{-n^2\pi^2+4i\tilde{\omega}}\right)\right)\sin n\pi\tilde{x}\\&=\sum_{m=1}^{\infty}\left(-\left(\frac{\dfrac{\partial p}{\partial z}}{\left(\dfrac{\partial p}{\partial z}\right)_0}\right)\left(\frac{16(1-(-1)^m)(1-i\tilde{\omega}\tilde{t}_r)}{m\pi(-m^2\pi^2(2N+1)^2+4i\tilde{\omega}(1-i\tilde{\omega}\tilde{t}_r))}\right)+c_{3,j,m}\cos\left(\frac{1}{2f\chi}\sqrt{-m^2\pi^2(2N+1)^2+4i\tilde{\omega}(1-i\tilde{\omega}\tilde{t}_r)}\right)\right.\\&\quad\left.+\,c_{4,j,m}\sin\left(\frac{1}{2f\chi}\sqrt{-m^2\pi^2(2N+1)^2+4i\tilde{\omega}(1-i\tilde{\omega}\tilde{t}_r)}\right)\right)\sin\left(m\pi(2N+1)(\tilde{x}-\tilde{x}_{ini,j})\right),\quad \text{if } \tilde{x}_{ini,j}\le\tilde{x}\le\tilde{x}_{fin,j}\quad \text{for } j=2,4,\ldots,2N,\end{aligned}\tag{27}$$

$$\begin{aligned}&\sum_{n=1}^{\infty}\left(-\left(\frac{\dfrac{\partial p}{\partial z}}{\left(\dfrac{\partial p}{\partial z}\right)_0}\right)\left(\frac{16(1-(-1)^n)}{n\pi(-n^2\pi^2+4i\tilde{\omega})}\right)+c_{1,n}\cos\left(-\frac{1}{2\chi}\sqrt{-n^2\pi^2+4i\tilde{\omega}}\right)+c_{2,n}\sin\left(-\frac{1}{2\chi}\sqrt{-n^2\pi^2+4i\tilde{\omega}}\right)\right)\sin n\pi\tilde{x}=0,\\&\quad\text{if } \tilde{x}_{ini,j}\le\tilde{x}\le\tilde{x}_{fin,j}\quad \text{for } j=1,3,\ldots,2N+1,\end{aligned}\tag{28}$$

while the continuity of the shear stress component acting on the plane of the bulk–nanocavity interface is given by

$$\begin{aligned}&\sum_{n=1}^{\infty}\frac{1}{\chi}\sqrt{-n^2\pi^2+4i\tilde{\omega}}\left(-c_{1,n}\sin\left(-\frac{1}{2\chi}\sqrt{-n^2\pi^2+4i\tilde{\omega}}\right)+c_{2,n}\cos\left(-\frac{1}{2\chi}\sqrt{-n^2\pi^2+4i\tilde{\omega}}\right)\right)\sin n\pi\tilde{x}\\&=\left(\frac{1}{1-i\tilde{\omega}\tilde{t}_r}\right)\sum_{m=1}^{\infty}\frac{1}{\chi}\sqrt{-m^2\pi^2(2N+1)^2+4i\tilde{\omega}(1-i\tilde{\omega}\tilde{t}_r)}\left(-c_{3,j,m}\sin\left(\frac{1}{2f\chi}\sqrt{-m^2\pi^2(2N+1)^2+4i\tilde{\omega}(1-i\tilde{\omega}\tilde{t}_r)}\right)\right.\\&\quad\left.+\,c_{4,j,m}\cos\left(\frac{1}{2f\chi}\sqrt{-m^2\pi^2(2N+1)^2+4i\tilde{\omega}(1-i\tilde{\omega}\tilde{t}_r)}\right)\right)\sin\left(m\pi(2N+1)(\tilde{x}-\tilde{x}_{ini,j})\right),\quad \text{if } \tilde{x}_{ini,j}\le\tilde{x}\le\tilde{x}_{fin,j}\quad \text{for } j=2,4,\ldots,2N.\end{aligned}\tag{29}$$

A. Strategy for the solution of the coupling between main and nano-channels

In order to determine the coefficients $c_{1,n}$, $c_{2,n}$, $c_{3,j,n}$, and $c_{4,j,n}$ using the boundary conditions given in Eqs. (24) and (26)–(29), it is necessary to carry out a change of basis set to solve such sum expressions, term by term. In this work, it is proposed to decompose each basis set function $\sin m\pi(2N+1)(\tilde{x}-\tilde{x}_{j,ini})$ in terms of the main channel basis set functions, given by $\{\sin(n\pi\tilde{x})\}$. The change of basis for each function $\sin(m\pi(2N+1)(\tilde{x}-\tilde{x}_{j,ini}))$ is given by the following expressions:

$$\sum\nolimits_{n=1}^{\infty}\varphi_{m,j,n}\sin n\pi\tilde{x}=\begin{cases}\sin(m\pi(2N+1)(\tilde{x}-\tilde{x}_{j,ini})), & \text{if } \tilde{x}_{ini,j}\le\tilde{x}\le\tilde{x}_{fin,j},\\ 0, & \text{elsewhere},\end{cases}\tag{30}$$

where each coefficient $\varphi_{m,j,n}$ is computed via the Fourier series of the right hand side of Eq. (30), as follows:

$$\varphi_{m,j,n}=\begin{cases}\dfrac{\cos(m\pi(j-1))}{2N+1}, & \text{if } n=(2N+1)m,\\[2ex] \dfrac{2m(2N+1)}{\pi(m^2(2N+1)^2-n^2)}\left(\sin\left(\dfrac{n\pi(j-1)}{2N+1}\right)-(-1)^m\sin\left(\dfrac{n\pi j}{2N+1}\right)\right), & \text{if } n\neq(2N+1)m.\end{cases}\tag{31}$$

Thus, when $\varphi_{m,j,n}$ is substituted from Eq. (31) in the boundary conditions given by Eqs. (27) and (28), it leads to the following expression of continuity of flow velocity, separated for each term $\sin n\pi\tilde{x}$:

$$-\left(\frac{\dfrac{\partial p}{\partial z}}{\left(\dfrac{\partial p}{\partial z}\right)_0}\right)\left(\frac{16(1-(-1)^n)}{n\pi(-n^2\pi^2+4i\tilde{\omega})}\right)+c_{1,n}\cos\left(-\frac{1}{2\chi}\sqrt{-n^2\pi^2+4i\tilde{\omega}}\right)+c_{2,n}\sin\left(-\frac{1}{2\chi}\sqrt{-n^2\pi^2+4i\tilde{\omega}}\right)$$

$$= \sum_{m=1}^{\infty}\sum_{j=2,even}^{2N}\left(-\left(\frac{\frac{\partial p}{\partial z}}{\left(\frac{\partial p}{\partial z}\right)_0}\right)\left(\frac{16(1-(-1)^m)(1-i\tilde{\omega}\tilde{t}_r)}{m\pi(-m^2\pi^2(2N+1)^2+4i\tilde{\omega}(1-i\tilde{\omega}\tilde{t}_r))}\right)+c_{3,j,m}\cos\left(\frac{1}{2f\chi}\sqrt{-m^2\pi^2(2N+1)^2+4i\tilde{\omega}(1-i\tilde{\omega}\tilde{t}_r)}\right)\right.$$
$$\left.+c_{4,j,m}\sin\left(\frac{1}{2f\chi}\sqrt{-m^2\pi^2(2N+1)^2+4i\tilde{\omega}(1-i\tilde{\omega}\tilde{t}_r)}\right)\right)\varphi_{m,j,n},\quad \text{for } n=1,2,3,\ldots, \tag{32}$$

and, accordingly, when $\varphi_{m,j,n}$ is substituted from Eq. (31) in Eq. (29), the following expression is obtained for continuity of shear stress:

$$\sqrt{-n^2\pi^2+4i\tilde{\omega}}\left(-c_{1,n}\sin\left(-\frac{1}{2\chi}\sqrt{-n^2\pi^2+4i\tilde{\omega}}\right)+c_{2,n}\cos\left(-\frac{1}{2\chi}\sqrt{-n^2\pi^2+4i\tilde{\omega}}\right)\right)$$
$$=\left(\frac{1}{1-i\tilde{\omega}\tilde{t}_r}\right)\sum_{m=1}^{\infty}\sum_{j=2,even}^{2N}\sqrt{-m^2\pi^2(2N+1)^2+4i\tilde{\omega}(1-i\tilde{\omega}\tilde{t}_r)}\left(-c_{3,j,m}\sin\left(\frac{1}{2f\chi}\sqrt{-m^2\pi^2(2N+1)^2+4i\tilde{\omega}(1-i\tilde{\omega}\tilde{t}_r)}\right)\right.$$
$$\left.+c_{4,j,m}\cos\left(\frac{1}{2f\chi}\sqrt{-m^2\pi^2(2N+1)^2+4i\tilde{\omega}(1-i\tilde{\omega}\tilde{t}_r)}\right)\right)\varphi_{m,j,n},\quad \text{for } n=1,2,3,\ldots. \tag{33}$$

In principle, Eqs. (24), (26), (32), and (33) are solvable as a linear system of algebraic equations for coefficients $c_{1,n}$, $c_{2,n}$, $c_{3,j,m}$, and $c_{4,j,m}$ by taking proper truncations on the sums over the indexes n and m, leading to a consistent truncated system of equations, as large as required to achieve convergence and accuracy of the results. However, this procedure is computationally unachievable when the main and subchannels differ in orders of magnitude, leading to a large value of the number of subchannels N. For this reason, a strategy of solution for coefficients $c_{4,j,m}$ that works properly for arbitrarily large values of N is proposed in this work. Such property is of importance for flow systems where nanometric subchannels are coupled with a main microchannel of size on the order of micrometers and larger. Such procedure is detailed now.

B. Considerations for an accurate solution at discrepant scales

As a first step to achieve a solution for an arbitrarily large number of subchannels N, the number of variables in the algebraic system is reduced as much as possible. To do so, Eq. (24) is solved for the coefficient $c_{1.n}$ as a function of $c_{2.n}$. In addition, Eq. (26) is solved for the coefficient $c_{3,j,m}$ as a function of $c_{4,j,m}$. Then, $c_{1,n}$ and $c_{3,j,m}$ are substituted in Eq. (32), leading to

$$\sum_{m=1}^{\infty}\sum_{j=2,even}^{2N}c_{4,j,m}\sin\left(\frac{1}{2f\chi}\sqrt{-m^2\pi^2(2N+1)^2+4\tilde{\omega}(i+\tilde{\omega}\tilde{t}_r)}\right)\varphi_{m,j,n}+c_{2,n}\sin\left(\frac{1}{2\chi}\sqrt{-n^2\pi^2+4i\tilde{\omega}}\right)=0,\quad \text{for } n=1,2,3,\ldots, \tag{34}$$

and, accordingly, $c_{1,n}$ and $c_{3,j,m}$ are substituted in Eq. (33), leading to

$$\left(\frac{\frac{\partial p}{\partial z}}{\left(\frac{\partial p}{\partial z}\right)_0}\right)\left(\frac{16(1-(-1)^n)\tan\left(\frac{1}{2\chi}\sqrt{-n^2\pi^2+4i\tilde{\omega}}\right)}{n\pi\chi\sqrt{-n^2\pi^2+4i\tilde{\omega}}}\right)+c_{2,n}\left(\frac{\sqrt{-n^2\pi^2+4i\tilde{\omega}}}{\chi}\right)\left(\frac{\cos\left(\frac{\sqrt{-n^2\pi^2+4i\tilde{\omega}}}{\chi}\right)}{\cos\left(\frac{\sqrt{-n^2\pi^2+4i\tilde{\omega}}}{2\chi}\right)}\right)$$
$$+\sum_{m=1}^{\infty}\sum_{j=2,even}^{2N}\left(\left(\frac{\frac{\partial p}{\partial z}}{\left(\frac{\partial p}{\partial z}\right)_0}\right)\left(\frac{16(1-(-1)^m)\tan\left(\frac{1}{2f\chi}\sqrt{-m^2\pi^2(2N+1)^2+4\tilde{\omega}(i+\tilde{\omega}\tilde{t}_r)}\right)}{m\pi\chi\sqrt{-m^2\pi^2(2N+1)^2+4\tilde{\omega}(i+\tilde{\omega}\tilde{t}_r)}}\right)\right.$$
$$\left.-c_{4,j,m}\left(\frac{\sqrt{-m^2\pi^2(2N+1)^2+4\tilde{\omega}(i+\tilde{\omega}\tilde{t}_r)}}{\chi(1-i\tilde{\omega}\tilde{t}_r)}\right)\left(\frac{\cos\left(\frac{1}{f\chi}\sqrt{-m^2\pi^2(2N+1)^2+4\tilde{\omega}(i+\tilde{\omega}\tilde{t}_r)}\right)}{\cos\left(\frac{1}{2f\chi}\sqrt{-m^2\pi^2(2N+1)^2+4\tilde{\omega}(i+\tilde{\omega}\tilde{t}_r)}\right)}\right)\right)\times\varphi_{m,j,n}=0,\quad \text{for } n=1,2,3,\ldots. \tag{35}$$

Finally, Eq. (34) is solved for the coefficient $c_{2,n}$ and substituted in Eq. (35), leading to the following expression:

$$\sum_{m=1}^{\infty}\sum_{j=2,even}^{2N}\left(-\frac{1}{\chi}\left(\frac{\sqrt{-m^2\pi^2(2N+1)^2+4\tilde{\omega}(i+\tilde{\omega}\tilde{t}_r)}}{1-i\tilde{\omega}\tilde{t}_r}\frac{\cos\left(\frac{1}{f\chi}\sqrt{-m^2\pi^2(2N+1)^2+4\tilde{\omega}(i+\tilde{\omega}\tilde{t}_r)}\right)}{\cos\left(\frac{1}{2f\chi}\sqrt{-m^2\pi^2(2N+1)^2+4\tilde{\omega}(i+\tilde{\omega}\tilde{t}_r)}\right)}\right.\right.$$
$$\left.\left.+2\sqrt{4i\tilde{\omega}-n^2\pi^2}\cot\left(\frac{\sqrt{4i\tilde{\omega}-n^2\pi^2}}{\chi}\right)\sin\left(\frac{\sqrt{4\tilde{\omega}(i+\tilde{\omega}\tilde{t}_r)-m^2\pi^2(2N+1)^2}}{2f\chi}\right)\right)\right)\varphi_{m,j,n}\,c_{4,j,m}$$
$$=\sum_{m=1}^{\infty}\sum_{j=2,even}^{2N}\left(-\left(\frac{\frac{\partial p}{\partial z}}{\left(\frac{\partial p}{\partial z}\right)_0}\right)\frac{16(1-(-1)^m)\tan\left(\frac{1}{2f\chi}\sqrt{4i\tilde{\omega}(1-i\tilde{\omega}\tilde{t}_r)-m^2\pi^2(2N+1)^2}\right)}{m\pi\chi\sqrt{-m^2\pi^2(2N+1)^2+4i\tilde{\omega}(1-i\tilde{\omega}\tilde{t}_r)}}\varphi_{m,j,n}\right)$$
$$-\left(\frac{\frac{\partial p}{\partial z}}{\left(\frac{\partial p}{\partial z}\right)_0}\right)\frac{16(1-(-1)^n)\tan\left(\frac{1}{2\chi}\sqrt{-n^2\pi^2+4i\tilde{\omega}}\right)}{n\pi\chi\sqrt{-n^2\pi^2+4i\tilde{\omega}}},\quad \text{for }\ n=1,2,3,\ldots. \tag{36}$$

Afterward, it is useful to recall that the system of study exhibits a specular symmetry along the YZ plane given by $\tilde{x}=\frac{1}{2}$. The symmetry of the solution establishes a relationship between the modes and flow rate in subchannels equidistant from the central plane, in the following way:

$$c_{4,2N-j+2,m}=(-1)^{m+1}c_{4,j,m},\quad \text{for }\ j=2,4,\ldots,N\quad\text{and}\quad m=1,2,3,\ldots, \tag{37}$$

which reduces the order of sum over index j in Eq. (36) by a half; thus, the number of variables is reduced accordingly, as follows:

$$\sum_{m=1}^{\infty}\sum_{j=2,even}^{N}\left(-\frac{1}{\chi}\left(\frac{\sqrt{-m^2\pi^2(2N+1)^2+4\tilde{\omega}(i+\tilde{\omega}\tilde{t}_r)}}{1-i\tilde{\omega}\tilde{t}_r}\frac{\cos\left(\frac{1}{f\chi}\sqrt{-m^2\pi^2(2N+1)^2+4\tilde{\omega}(i+\tilde{\omega}\tilde{t}_r)}\right)}{\cos\left(\frac{1}{2f\chi}\sqrt{-m^2\pi^2(2N+1)^2+4\tilde{\omega}(i+\tilde{\omega}\tilde{t}_r)}\right)}\right.\right.$$
$$\left.\left.+2\sqrt{-n^2\pi^2+4i\tilde{\omega}}\cot\left(\frac{\sqrt{-n^2\pi^2+4i\tilde{\omega}}}{\chi}\right)\sin\left(\frac{\sqrt{-m^2\pi^2(2N+1)^2+4\tilde{\omega}(i+\tilde{\omega}\tilde{t}_r)}}{2f\chi}\right)\right)\right)(\varphi_{m,j,n}+(-1)^{m+1}\varphi_{m,2N-j+2,n})c_{4,j,m}$$
$$=-\left(\frac{\frac{\partial p}{\partial z}}{\left(\frac{\partial p}{\partial z}\right)_0}\right)\sum_{m=1}^{\infty}\sum_{j=2,even}^{2N}\left(\frac{16(1-(-1)^m)\tan\left(\frac{1}{2f\chi}\sqrt{4i\tilde{\omega}(1-i\tilde{\omega}\tilde{t}_r)-m^2\pi^2(2N+1)^2}\right)}{m\pi\chi\sqrt{-m^2\pi^2(2N+1)^2+4i\tilde{\omega}(1-i\tilde{\omega}\tilde{t}_r)}}\varphi_{m,j,n}\right)$$
$$-\left(\frac{\frac{\partial p}{\partial z}}{\left(\frac{\partial p}{\partial z}\right)_0}\right)\frac{16(1-(-1)^n)\tan\left(\frac{1}{2\chi}\sqrt{-n^2\pi^2+4i\tilde{\omega}}\right)}{n\pi\chi\sqrt{-n^2\pi^2+4i\tilde{\omega}}},\quad \text{for }\ n=1,2,3,\ldots. \tag{38}$$

The next step is a rescaling of variable $c_{4,j,m}$ in Eq. (38), since the elements of matrix for its solution grow exponentially for large values of index m. To avoid such difficulty in matrix computations, the following change of variable is carried out:

$$c^{red}_{4,j,m}=c_{4,j,m}\,\exp\left(-\frac{i}{2f\chi}\sqrt{-m^2\pi^2(2N+1)^2+4\tilde{\omega}(i+\tilde{\omega}\tilde{t}_r)}\right). \tag{39}$$

The final step for the solution of the system of equations given by Eq. (38) requires a rotation of the matrix. To do so, the following basis set, denoted by $d_{4,k,m}$, is shown:

$$d_{4,k,m}=\sum_{j=2,j\,even}^{N}\left(\left(\frac{1-(-1)^m}{2}\right)\sin\frac{k\pi\left(j-\frac{1}{2}\right)}{2N+1}+\left(\frac{1+(-1)^m}{2}\right)\cos\frac{k\pi\left(j-\frac{1}{2}\right)}{2N+1}\right)c^{red}_{4,j,m},\quad \text{for } k=1,3,\ldots,N-1 \text{ and } m=1,2,\ldots, \tag{40}$$

which can be substituted in the system of equations given by Eqs. (38) and (39). This is carried out by the conventional methods of linear algebra, as summarized below. Notice that the coefficient k runs over odd numbers only, as a consequence of the reduction of variables done in Eq. (37).

The procedure to simplify the system of equations requires the inversion of the matrix associated with Eq. (40). It is important to point out that the transformation defined in Eq. (40) is invertible, since its determinant is nonsingular for all positive integer values of N. As an example, for odd values of m, such determinant is given by

$$\Delta = \det\begin{vmatrix} \sin\dfrac{\pi(2(2)-1)}{2(2N+1)} & \sin\dfrac{\pi(2(4)-1)}{2(2N+1)} & \cdots & \sin\dfrac{\pi(2N-1)}{2(2N+1)} \\ \sin\dfrac{3\pi(2(2)-1)}{2(2N+1)} & \sin\dfrac{3\pi(2(4)-1)}{2(2N+1)} & \cdots & \sin\dfrac{3\pi(2N-1)}{2(2N+1)} \\ \vdots & \vdots & \ddots & \vdots \\ \sin\dfrac{(N-1)\pi(2(2)-1)}{2(2N+1)} & \sin\dfrac{(N-1)\pi(2(4)-1)}{2(2N+1)} & \cdots & \sin\dfrac{(N-1)\pi(2N-1)}{2(2N+1)} \end{vmatrix}. \tag{41}$$

Then, the matrix associated with the system of equations in Eq. (38) is rescaled by Eq. (39) and then transformed according to Eq. (40), which results in a transformed system of equations, as follows:

$$\begin{aligned} \sum_{m=1}^{\infty}\sum_{k=1,odd}^{N-1} A_{n,m,k}d_{4,k,m} = &-\left(\frac{\dfrac{\partial p}{\partial z}}{\left(\dfrac{\partial p}{\partial z}\right)_0}\right)\frac{16(1-(-1)^n)\tan\left(\dfrac{1}{2\chi}\sqrt{-n^2\pi^2+4i\tilde{\omega}}\right)}{n\pi\chi\sqrt{-n^2\pi^2+4i\tilde{\omega}}} - \left(\frac{\dfrac{\partial p}{\partial z}}{\left(\dfrac{\partial p}{\partial z}\right)_0}\right) \\ &\times\sum_{m=1}^{\infty}\sum_{j=2,even}^{2N}\left(\frac{16(1-(-1)^m)\tan\left(\dfrac{1}{2f\chi}\sqrt{4i\tilde{\omega}(1-i\tilde{\omega}\tilde{t}_r)-m^2\pi^2(2N+1)^2}\right)}{m\pi\chi\sqrt{-m^2\pi^2(2N+1)^2+4i\tilde{\omega}(1-i\tilde{\omega}\tilde{t}_r)}}\varphi_{m,j,n}\right), \quad \text{for } n = 1,2,3,\ldots, \end{aligned} \tag{42}$$

where each term $A_{n,m,k}$ is computed by inversion of the matrix associated with Eq. (40). In order to show a useful property of this transformation, some algebraic details are presented now. They are exemplified for the case of any odd value of m. However, an analogous derivation can be carried out for any even value of m. Following the conventional methods of linear algebra, each term $A_{n,m,k}$ is of the form:

$$\begin{aligned} A_{n,m,k} \propto (\varphi_{m,2,n}+\varphi_{m,2N,n})\det&\begin{vmatrix} \delta_{k,1} & \sin\dfrac{\pi(2(4)-1)}{2(2N+1)} & \cdots & \sin\dfrac{\pi(2N-1)}{2(2N+1)} \\ \delta_{k,3} & \sin\dfrac{3\pi(2(4)-1)}{2(2N+1)} & \cdots & \sin\dfrac{3\pi(2N-1)}{2(2N+1)} \\ \vdots & \vdots & \ddots & \vdots \\ \delta_{k,N-1} & \sin\dfrac{(N-1)\pi(2(4)-1)}{2(2N+1)} & \cdots & \sin\dfrac{(N-1)\pi(2(N)-1)}{2(2N+1)} \end{vmatrix} \\ +(\varphi_{m,4,n}+\varphi_{m,2N-2,n})\det&\begin{vmatrix} \sin\dfrac{\pi(2(2)-1)}{2(2N+1)} & \delta_{k,1} & \cdots & \sin\dfrac{\pi(2N-1)}{2(2N+1)} \\ \sin\dfrac{3\pi(2(2)-1)}{2(2N+1)} & \delta_{k,3} & \cdots & \sin\dfrac{3\pi(2N-1)}{2(2N+1)} \\ \vdots & \vdots & \ddots & \vdots \\ \sin\dfrac{(N-1)\pi(2(2)-1)}{2(2N+1)} & \delta_{k,N-1} & \cdots & \sin\dfrac{(N-1)\pi(2(N)-1)}{2(2N+1)} \end{vmatrix} + \cdots \\ +(\varphi_{m,N,n}+\varphi_{m,N+2,n})\det&\begin{vmatrix} \sin\dfrac{\pi(2(2)-1)}{2(2N+1)} & \sin\dfrac{\pi(2(4)-1)}{2(2N+1)} & \cdots & \delta_{k,1} \\ \sin\dfrac{3\pi(2(2)-1)}{2(2N+1)} & \sin\dfrac{3\pi(2(4)-1)}{2(2N+1)} & \cdots & \delta_{k,3} \\ \vdots & \vdots & \ddots & \vdots \\ \sin\dfrac{(N-1)\pi(2(2)-1)}{2(2N+1)} & \sin\dfrac{(N-1)\pi(2(4)-1)}{2(2N+1)} & \cdots & \delta_{k,N-1} \end{vmatrix} \\ &\text{for } k = 1,3,5,\ldots,N-1,\ \ n = 1,2,3,\ldots \text{ and } m = 1,3,5,\ldots. \end{aligned} \tag{43}$$

where $\delta_{k,1}$, $\delta_{k,3}$, $\delta_{k,N\text{-}1}$ stand for the Kronecker delta. A thorough numerical analysis and testing of Eq. (43) unveils that there are specific choices of n that make the coefficients $A_{n,k,m}$ vanish for all values of k except one. Specifically, if the nonvanishing coefficients correspond to the value $k = k_0$, the complete set of values of n is shown as follows:

$$\begin{aligned} n \in \{&k_0, (2N+1)(1) - (k_0-1), (2N+1)(1) + k_0, (2N+1)(2) \\ &- (k_0-1), (2N+1)(2) + k_0, \\ &(2N+1)(3) - (k_0-1), (2N+1)(3) + k_0, \dots\}. \end{aligned} \tag{44}$$

The result presented in Eq. (44) holds for even values of m as well. Equivalent expressions to Eqs. (41) and (43) for even values of m have been omitted for sake of economy in space. It is important to notice that any positive value of n defines an equation to be solved for all the coefficients $d_{4,k,m}$; however, if it is chosen one of the values in Eq. (44), the resulting equation only depends on the coefficients $d_{n,k_0,m}$ for that specific value of k_0. In linear algebra terms, the transformation carried out in Eq. (42) with Eq. (44) produces a block diagonal matrix, where each specific subset of variables $\{d_{4,k_0,1}, d_{4,k_0,2}, \dots, d_{4,k_0,m}, \dots\}$ can be solved independently of the other values of k. Consequently, an adequate choice of index n considerably simplifies the solution of the system of algebraic equations, because the size of each diagonal block depends only on the number of terms for index m, and not on the number of subchannels N. This is a fundamental requirement to create a robust framework for the analytical solution presented, such that the solution does not scale with the number of subchannels and can be employed regardless of the discrepancy between main and subchannel sizes. This property ensures that the computation of a solution is achievable for arbitrarily large values of N, from a theoretical and computational point of view.

In practical terms, considering sums over m truncated up to M, and considering N subchannels, Eq. (38) requires to solve a large and complex $\frac{MN}{2} \times \frac{MN}{2}$ system of equations; however, after transformation in Eq. (40), the system is transformed into $\frac{N}{2}$ independent systems of equations, each of size $M \times M$ and associated with a specific value of $k = k_0$. For each reduced system of algebraic equations, it is possible to solve for the coefficients $\{d_{4,k_0,1}, d_{4,k_0,2}, \dots, d_{4,k_0,M}\}$. Following this treatment, the solution is given by the tools of linear algebra available in most of advance programming packages. In this work, Wolfram Mathematica utilities were employed for this purpose. The code developed to summarize this methodology is available under an open source license on GitHub (see Appendix B).

IV. EFFECT OF NANOSCALE/MICROSCALE COUPLING: VISCOELASTIC RESONANCES AT THE INTERFACE

Three quantities are computed in order to summarize the findings of the analytical solution in the three main elements of the flow system. First, the flow rate in the main channel is given by

$$\hat{Q}_I(\tilde{\omega}) = \int_{\tilde{x}=0}^{\tilde{x}=1} \int_{\tilde{y}=-\frac{1}{2}}^{\tilde{y}=\frac{1}{2}} \hat{v}_I(\tilde{x},\tilde{y},\tilde{\omega})\, d\tilde{y}\, d\tilde{x}\,. \tag{45}$$

Second, the average flow rate in the subchannels is given by

$$\hat{Q}_{II}^{net}(\tilde{\omega}) = \frac{1}{N} \sum_{j=2,even}^{2N} \left(\frac{f}{\tilde{x}_{fin,j} - \tilde{x}_{ini,j}} \int_{\tilde{x}=\tilde{x}_{ini,j}}^{\tilde{x}=\tilde{x}_{fin,j}} \int_{\tilde{y}=-\frac{1}{2f}}^{\tilde{y}=\frac{1}{2f}} \hat{v}_I(\tilde{x},\tilde{y},\tilde{\omega})\, d\tilde{y}\, d\tilde{x} \right). \tag{46}$$

Finally, the average flow velocity at the interface between the main channel and the subchannels is given by

$$\hat{v}_I^{x-ave}\left(\tilde{y} = -\frac{1}{2}, \tilde{\omega}\right) = \int_{\tilde{x}=0}^{\tilde{x}=1} \hat{v}_I\left(\tilde{x}, \tilde{y} = -\frac{1}{2}, \tilde{\omega}\right) d\tilde{x}. \tag{47}$$

With these quantities, the frequency spectrum of the system is summarized in Fig. 2. From this figure on, representative values of the properties of microchannel are considered. In most cases, main channel width and height are of 1 μm, subchannels width and height are of 4 nm while water density and viscosity are approximated to 1000 kg m^{-3} and 0.001 Pa s, respectively. In consequence,

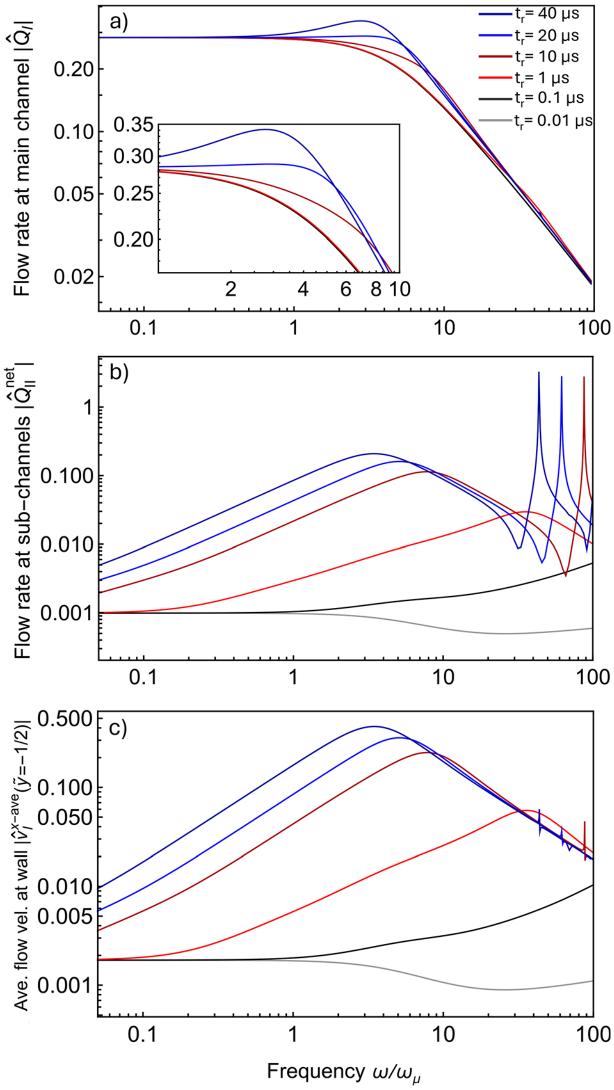

FIG. 2. Frequency spectrum of (a) dimensionless water flow rate in the main channel, (b) average value of dimensionless flow rate in subchannels, (c) average flow velocity at the rough interface. Width and height of main channel is 1 μm. Width and height of sub channels is 4 nm. Different relaxation times at the subchannels are considered in the same range of values measured by Kapoor *et al.* (2014).

the characteristic frequency of the spectrum corresponds to a viscous frequency of $\omega_\mu = 4 \times 10^6$ rad s^{-1}.

The response of each element of the system to different frequencies share some features. Flow rate in main channel [Fig. 2(a)], at the average of subchannels [Fig. 2(b)] and flow velocity at the interface [Fig. 2(c)] present clear peaks at certain frequencies, namely, resonances. The first resonance is clear and strong in all the elements of the system, both at channels and at the interface. However, the subsequent resonances are only prominent at subchannels, as shown in Fig. 2(b).

It is also clear that the increase in flow rate and flow velocity depends on the magnitude of relaxation time; relaxation times smaller than the ones encountered by Kapoor *et al.*, 2014, which are on the order of tenths of microseconds, lead to a very small change in flow properties of the microchannel. In such regard, it is clear that relaxation times measured by Kapoor *et al.* (2014) produce a very strong effect on the response of the microfluidic channel, much larger than Newtonian fluids that could be considered similar to the curves with the lowest relaxation time values in Fig. 2.

The occurrence of flow rate resonances in the subchannels is consistent with viscoelastic resonances obtained theoretically and experimentally in pulsatile microfluidic devices (Vazquez-Vergara *et al.*, 2021b; 2021a), and it is understandable as a resonance of the characteristic time of the elastic component of the rheological response of the fluid, interacting with the pulsatile pressure gradient under nanometric conditions. However, it is important to understand and describe in more detail the propagation of such a resonance, from its origin at the subchannels, to the interface and to the main microchannel. In order to understand this nonmonotonic dependence with frequency, the spatial–temporal profile is depicted at four characteristic points in the frequency spectrum.

In order to compute the spatial–temporal profile of flow velocity, it is necessary to consider a specific form of the pressure gradient profile. In this work, it is considered a monomodal pressure gradient of the form

$$\frac{\partial p}{\partial z}(t) = \left(\frac{\partial p}{\partial z}\right)_0 \cos(\omega_0 t), \tag{48}$$

and, in consequence, the inverse Fourier transform of $\hat{v}_I$ and $\hat{v}_{II,j}$ leads to

$$\tilde{v}_p(\tilde{x}, \tilde{y}, \tilde{t}) = \mathrm{Re}\left(\hat{v}_p\left(\tilde{x}, \tilde{y}, \tilde{\omega} = \frac{\omega_0}{\omega_\mu}\right) \exp\left(-\frac{i\omega_0 \tilde{t}}{\omega_\mu}\right)\right), \tag{49}$$
$$\text{for } p = I \text{ and } II, j.$$

First, the flow velocity profile at a frequency lower than the main resonance is depicted in Fig. 3 (Multimedia available online). The main channel is shown to develop a classical parabolic profile where the rough interface exhibits a negligible slippage. In turn, a larger flow velocity is developed in the main microchannel, and it propagates from there to the subchannels, as observed when the maximum flow velocity is located in the proximity of the interface.

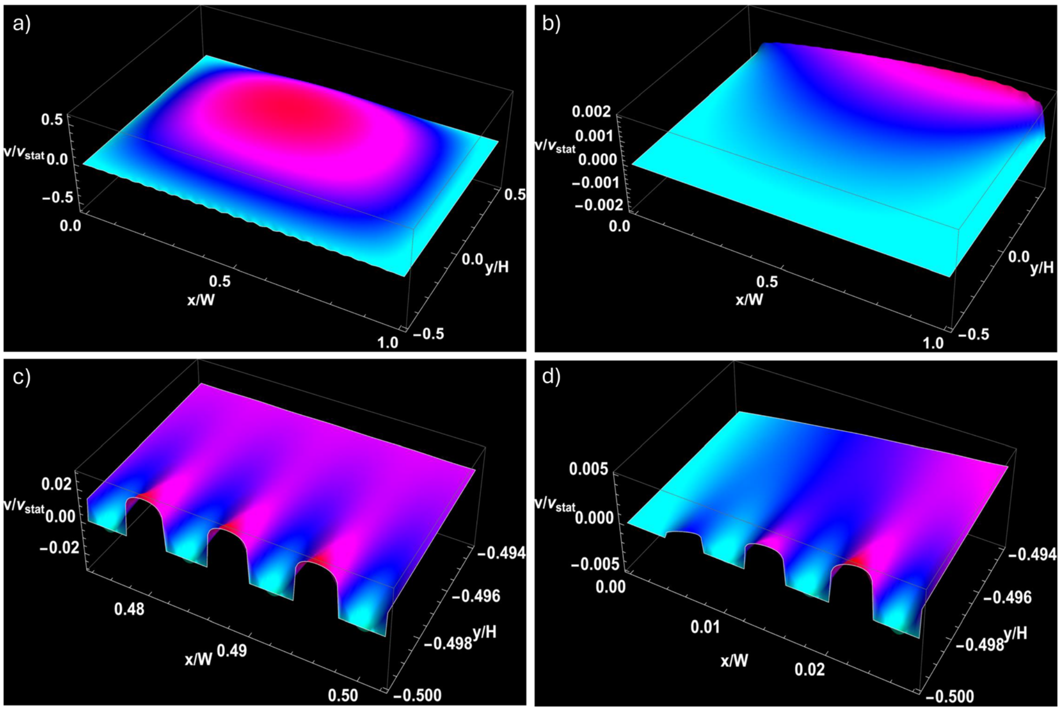

FIG. 3. Spatial and temporal profiles of flow velocity for a frequency of $\tilde{\omega} = 0.1$, at conditions below the first resonance. Relaxation time is 20 μs, dimensions of main channel are $1 \times 1\ \mu\text{m}^2$, and of each subchannel are $4 \times 4\,\text{nm}^2$. (a) Global view of the velocity field at the entire channel. (b) Global view of the velocity field at the subchannel located closest to the left wall. (c) Zoom-in view of flow velocity of main channel at the vicinity of the rough interface, at the center of the interface. (d) Zoom-in view of flow velocity of main channel at the vicinity the rough interface close to the left wall. Multimedia available online.

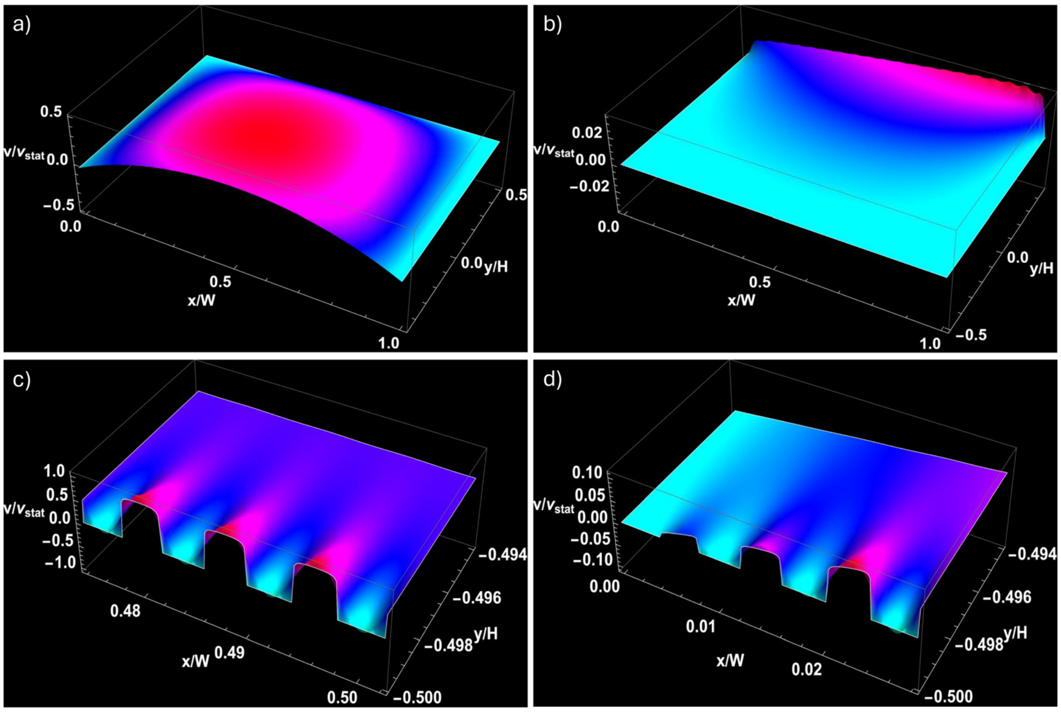

FIG. 4. Spatial and temporal profiles of flow velocity for a frequency of $\tilde{\omega} = 5.25$, at conditions close to the first resonance. Relaxation time is 20 μs, dimensions of main channel are $1 \times 1\ \mu m^2$, and of each subchannel are $4 \times 4\,nm^2$. (a) Global view of the velocity field at the entire channel. (b) Global view of the velocity field at the subchannel located closest to the left wall. (c) Zoom-in view of flow velocity of main channel at the vicinity the rough interface, at the center of the interface. (d) Zoom-in view of flow velocity of main channel at the vicinity the rough interface close to the left wall. Multimedia available online.

The flow velocity profile at the frequency of the first resonance is depicted in Fig. 4 (Multimedia available online). Despite the fact that the spatial dependence of the flow velocity at the main microchannel is still parabolic, a large slippage at the rough interface is observed. Moreover, such a resonance is very pronounced in the interface between the main channel and subchannels, there is no clear maximum of flow velocity in the bulk of subchannel flow. This is very important because it means that this resonance is produced mostly by the interaction of elastic waves that are propagated to the main microchannel and the interface, and this explains that the biggest increase in flow velocity occurs at the interface vicinity of the rough interface, not in the bulk of channels. In these terms, this prominent resonance is produced by coupling of the dimensions of the main microchannel with the viscoelasticity of subchannels. This is an emerging resonance that does not correspond to the resonances encountered previously, and it is a consequence of the interaction of a nanoconfined Maxwellian fluid with a Newtonian fluid confined in a larger space.

The flow velocity profile at the frequency that corresponds to the second resonance of flow rate in the subchannels is depicted in Fig. 5 (Multimedia available online). In contrast to the first resonance, the second resonance shows a clear maximum in the middle of each subchannel, which means that the resonance is produced by the bouncing of elastic waves only in the nanometric confinement, without a significant propagation to the larger dimension of the main microchannel. This explains the relatively low impact of the second resonance on the flow velocity in the interface and, subsequently, in the main microchannel.

Finally, the flow velocity profile at a frequency higher than the second resonance of flow rate in the subchannels is depicted in Fig. 6 (Multimedia available online). In such conditions, the velocity profile in the main microchannel is significantly flat, which is consistent with the expected results of flow velocity profiles at high values of the Womersley number, since each pressure cycle is too fast compared to the viscous characteristic time, and its short duration is insufficient for the formation of the parabolic profile (Torres-Herrera, 2021).

A global view of the spatial and temporal profiles provides a very important result: The large resonance at the rough interface can only be understood as a combined effect of elastic waves produced in the viscoelastic subchannels, which are propagated along the main channel, with much larger dimensions and without a viscoelastic response itself. Complex flow systems exhibit resonances where all dimensions are combined, and resonant waves are produced in one region and propagated in the rest of the system. Consequently, it is necessary to define minimal requirements for subchannels, namely, size and viscoelastic properties, that are sufficiently large to generate elastic waves for their propagation to the rest of the system, significantly modifying the flow dynamics. A thorough examination of these phenomena is given in Secs. V and VI.

V. FLOW AT THE INTERFACE AND SLIPPAGE

It is important to establish a comparison between these results and a simplified description of fluid/wall interfaces in terms of a slip boundary condition. For this purpose, the dynamics at the rough

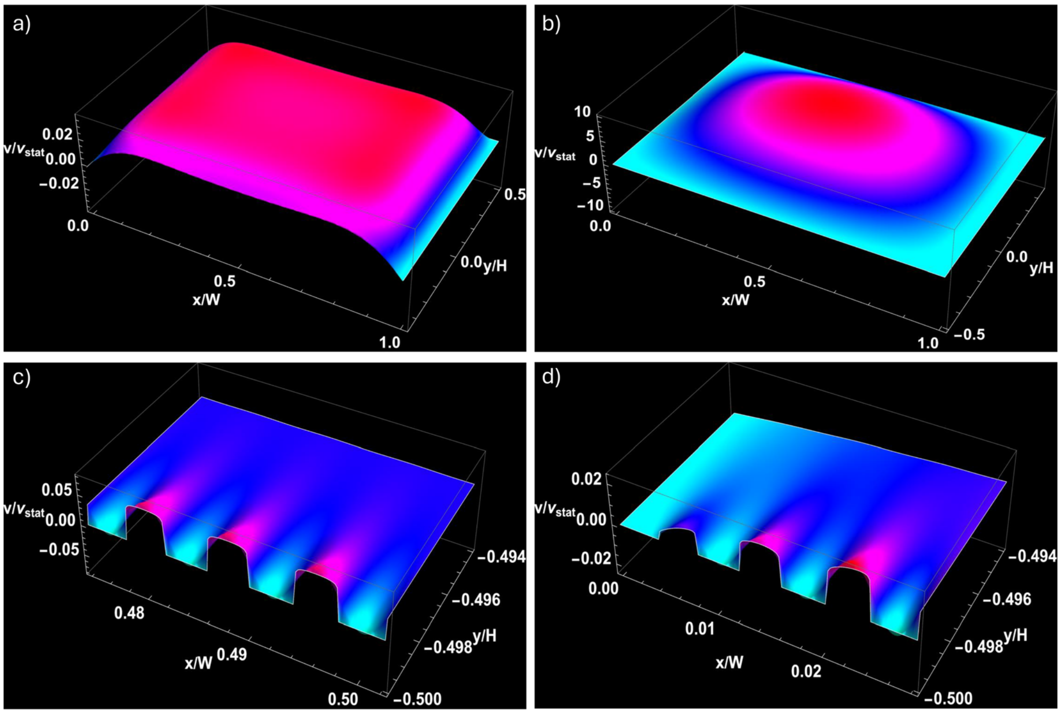

FIG. 5. Spatial and temporal profiles of flow velocity for a frequency of $\tilde{\omega} = 62.5$, at conditions close to the second resonance. Relaxation time is 20 μs, dimensions of main channel are 1×1 μm^2, and of each subchannel are 4×4 nm^2. (a) Global view of the velocity field at the entire channel. (b) Global view of the velocity field at the subchannel located closest to the left wall. (c) Zoom-in view of flow velocity of main channel at the vicinity the rough interface, at the center of the interface. (d) Zoom-in view of flow velocity of main channel at the vicinity the rough interface close to the left wall. Multimedia available online.

interface is described in terms of an effective slip length, defined consistently with Navier's hypothesis as follows:

$$\frac{\lambda_{eff}(\tilde{\omega})}{H_I} \equiv \frac{\left|\int_0^1 \hat{v}_I\left(\tilde{x}, \tilde{y} = -\frac{1}{2}, \tilde{\omega}\right) d\tilde{x}\right|}{\left|\int_0^1 \frac{\partial \hat{v}_I}{\partial \tilde{y}}\left(\tilde{x}, \tilde{y} = -\frac{1}{2}, \tilde{\omega}\right) d\tilde{x}\right|}. \qquad (50)$$

The slip length for different pulsation frequencies is summarized in Fig. 7. In contrast to the complex dependence of flow velocity at the interface with frequency shown in Fig. 2(c), effective slip length shows a simple trend for most frequencies. However, for large values of relaxation time, i.e., $t_r = 10$, 20, and 40 μs, effective slip length shows a punctual sudden reduction at large frequency values in a very narrow range of values. Such an anomalous reduction of slip length occurs close to the arising of second resonance. This is understandable since the second resonance occurs mostly at the subchannels and is not propagated to the main channel nor to the interface. In these terms, the gradient of flow velocity in the interface plane increases significantly due to the increase in flow velocity in the subchannel, but the flow velocity itself has not increased so far. This produces a much larger value of the denominator in Eq. (50), while the numerator remains mostly unchanged. The combined effect leads to a considerable decrease in the quotient, which explains the sudden reduction in slip length at the second resonance.

It is important to note that the effective slip length in the limit of small frequencies in Fig. 7 does not go to zero but reaches an asymptotic small value. This result is explained in terms of the contribution of each subchannel to a marginal increase in effective flow area. Even a Newtonian fluid in a nanocavity exhibits a flow velocity of a small magnitude. In turn, this produces a small flow velocity in the interface, leading to slip lengths that are approximately two orders of magnitude smaller than the width of the main channel.

A. Role of relaxation time and rugosity size

One of the main advantages of the proposed analytical solution is the possibility to extrapolate the results in the former sections and explore a wide range of physical conditions, beyond the relaxation times and confinement size range determined by Kapoor *et al.* (2014). The purpose of such a study is to survey a wide range of physical conditions in order to exploit these theoretical findings as a predictive tool.

With the aforementioned objective, an exploration of other sizes of microchannels is presented in Fig. 8. It is clear that the propagation of high amplitude elastic waves requires a certain amount of viscoelastic fluid in the subchannels, sufficient to transmit in an effective manner the elastic wave to the interface and subsequently to the main channel. This is inferred from the fact that an increase in subchannel width and height always leads to an increase in slip length. However, it

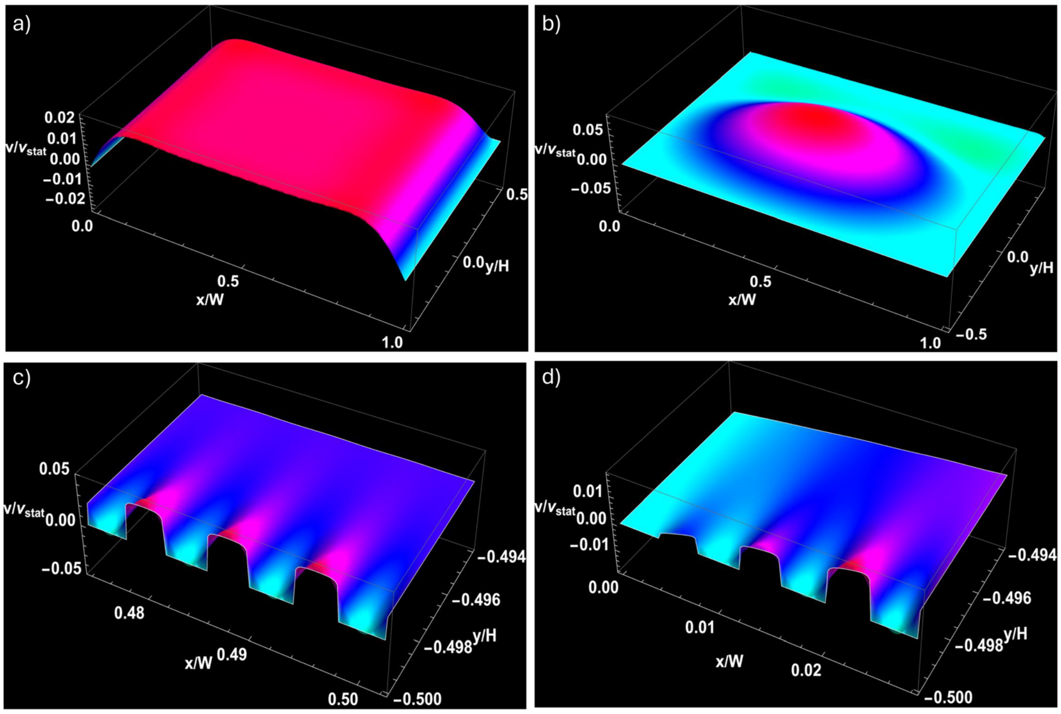

FIG. 6. Spatial and temporal profiles of flow velocity for a frequency of $\tilde{\omega} = 100.0$, at conditions above the second resonance. Relaxation time is 20 μs, dimensions of main channel are $1 \times 1\ \mu m^2$, and of each subchannel are $4 \times 4\,nm^2$. (a) Global view of the velocity field at the entire channel. (b) Global view of the velocity field at the subchannel located closest to the left wall. (c) Zoom-in view of flow velocity of main channel at the vicinity the rough interface, at the center of the interface. (d) Zoom-in view of flow velocity of main channel at the vicinity the rough interface close to the left wall. Multimedia available online.

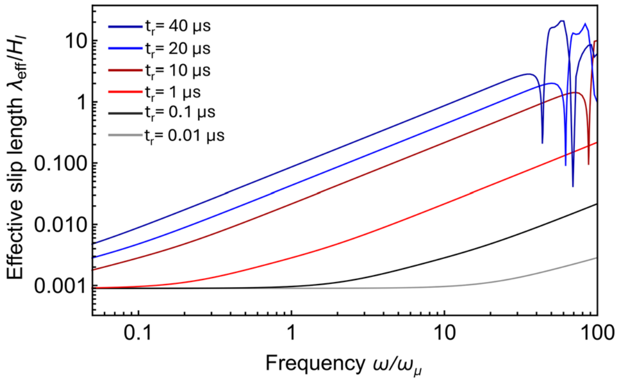

FIG. 7. Effective slip length as a function of pulsation frequency. Width and height of main channel are 1 μm. Width and height of subchannels are 4 nm. Different relaxation times at the subchannels are considered in the same range of values measured by Kapoor *et al.* (2014).

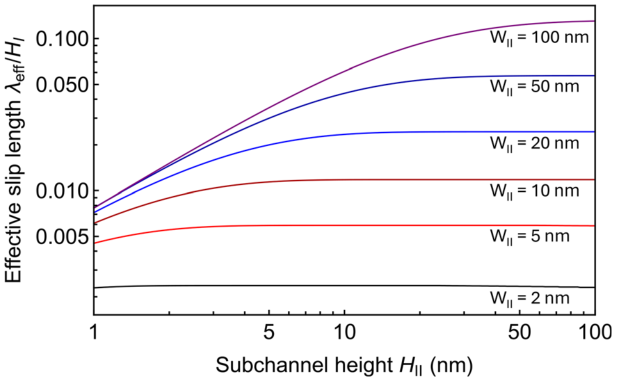

FIG. 8. Effective slip length as a function of subchannel width and height. A pulsation frequency of $\tilde{\omega} = 0.1$ and a relaxation time of $t_r = 20\ \mu$s are considered in all computations.

is also observed that when the subchannel width is fixed, an increase in the subchannel height produces a significant increase in slip length until a certain point; from then on, a further increase in subchannel height has a marginal effect on the effective slip length.

As a first step to understand the role of nanoconfined rheological behavior in the flow slippage predicted in this work, the exploration of a wide range of relaxation times is presented in Fig. 9. Specifically, Fig. 9(a) shows that, for sufficiently low values of relaxation time and pulsation frequency, slip length reaches a plateau where Newtonian behavior is observed; moreover, such a lower bound of slip length remains the same regardless of the pulsation frequency of nanoconfined water at the subchannels. This is understood in terms of the formation of a parabolic profile when the pulsation period is sufficiently large compared with the relaxation time; under such conditions, flow velocity is limited by the viscous component of Maxwellian shear

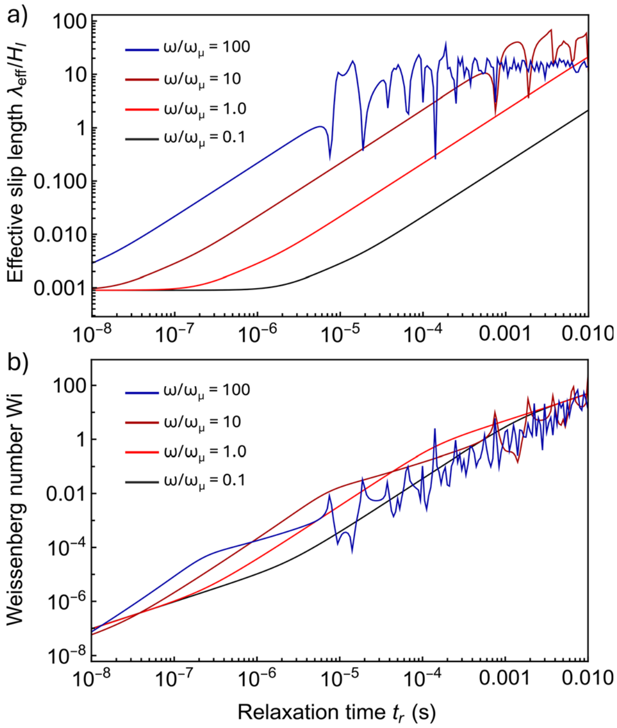

FIG. 9. Exploration of main features of viscoelastic behavior for different values of relaxation time of nanoconfined water. (a) Effective slip length and (b) the Weissenberg number as a function of relaxation time, considering $\left(\frac{\partial p}{\partial z}\right)_0 = -\frac{100\,\mathrm{Pa}}{0.01\,\mathrm{m}}$. Four characteristic pulsation frequencies are plotted. Main channel dimensions are $1 \times 1\,\mu\mathrm{m}^2$, subchannels dimensions are $4 \times 4\,\mathrm{nm}^2$ in all computations.

stress, which is identical to the shear stress of a Newtonian fluid with the same viscosity in the limit of low pulsation frequencies.

On the other hand, several abrupt changes in slip length are observed in Fig. 9 when relaxation time and pulsation frequency increase sufficiently. This is understood in terms of resonances produced in the subchannels that are not effectively propagated to the interface and to the main microchannel, as formerly mentioned in Sec. IV for large values of frequencies in Fig. 7. In this context, the emergence of multiple zones of anomalous slip length is translated to high-order resonances of the subchannels. It is noticeable that beyond each particular resonance, the envelope of the effective slip length reaches an asymptotic upper bound. This means that the increase in flow velocity at the interface and, hence, the enhance of flow slippage caused by nanoscale-emergent viscoelasticity, is limited to a certain upper bound. Beyond that point, an increase in the relaxation time and, thus, of the viscoelasticity of the nanoconfined fluid, will have no further effect on the flow velocity at the interface.

In order to define the range of validity of Maxwell's model of linear viscoelasticity, Fig. 9(b) exhibits low values of the Weissenberg number for relaxation times lower than 10^{-3} s for a representative high value of pressure gradient (details of the computation of Weissenberg number Wi are defined in Appendix A). A value of Wi lower than unit shows that the elastic response is linear and yet dominated by the viscous component of shear stress; it is also an indication that the nonlinear effects of viscoelastic behavior, such as shear thinning and increase in normal stress, are not expected to influence significantly the results observed for relaxation times lower than 10^{-3} s (Thompson and Oishi, 2021).

In addition to the discussion mentioned above, it is important to consider the complexity of size-dependent rheology. Width and height of nanochannels are always larger or equal to 2 nm in all computations of the present work. Under these conditions, the experimental results obtained by Kapoor *et al.* (2014) have demonstrated that shear thinning is minimal, and the rheological behavior is dominated by a single size-dependent relaxation time. In contrast, for confining dimensions smaller than 2 nm, a significant shear thinning dominates the rheological behavior. Such extremely low confining dimensions are beyond the scope of this work and deserve further exploration.

VI. CONCLUSIONS AND REMARKS

The emergence of viscoelastic behavior in nanoconfined water is a recent finding, whose consequences are yet to be completely understood in many fields where unsteady flow of water plays a key role. Within this context, one of such consequences has been explored in this work, which connects the viscoelasticity of water with an effective slippage caused by wall rugosity. Ultimately, such a finding impacts on the amplitude and spatial characteristics of flow velocity observed in pulsatile microfluidics of high-polarity channels.

From a conceptual point of view, the results obtained are useful for prediction of conditions of very high slippage at water/solid interfaces. However, from a practical/experimental point of view, it is important to mention that the predicted conditions for slip lengths of very high magnitude typically require pulsation frequencies of high magnitude as well. Since the characteristic frequency of resonances has been presented in dimensionless units in this work, a translation of such computations into dimensional quantities leads to resonance frequencies on the order of Kilohertz to Megahertz, depending on the size of the particular channel and rugosity in question. Therefore, the first steps for experimental investigation based on these results should focus on the region of moderate pulsation frequencies. Nevertheless, water viscoelasticity still produces an effective slip length of significant magnitude under such conditions.

As in any theoretical work, the results presented are intrinsically limited by the simplifications and approximations of the model, regarding the geometry of rough patterns as parallel equidistant rectangular subchannels. Certainly, a more realistic representation of rugosity must consider cavities of complex geometry and size variability, which impacts the cross-sectional area of each subchannel and produces a flow dependence with the axial coordinate. However, given the challenge of modeling the multiscale nature of rough or patterned surfaces in microfluidic components in full detail, it is useful to rely on analytical results that provide approximated or asymptotic results. In this regard, the results presented in this work could provide some guidelines for the design of experimental setups and for subsequent theoretical studies and simulations.

Flow slippage in micro and nanofluidic systems is an area where many fields of physics and chemistry converge. The results of this work can be interpreted as a consequence of the out-of-equilibrium interactions between water molecules and polar nanometric confinements, which produce an elastic response of water aggregates and ultimately lead to an effective flow slippage that could be of significant magnitude under specific conditions encountered in pulsatile microfluidics. It is necessary to advance toward a deeper, more detailed understanding of the phenomena at the interface of nano and microscale flow systems under dynamic situations. The capabilities of microfluidic and nanofluidic devices to observe and exploit these phenomena are constantly evolving.

ACKNOWLEDGMENTS

The author acknowledges financial support from Consejo Nacional de Humanidades, Ciencias y Tecnologías (CONAHCyT, Mexico) through Postdoctoral Fellowship (CVU 672448).

AUTHOR DECLARATIONS

Conflict of Interest

The author has no conflicts to disclose.

Author Contributions

Ulises Torres-Herrera: Conceptualization (equal); Data curation (equal); Formal analysis (equal); Funding acquisition (equal); Investigation (equal); Methodology (equal); Project administration (equal); Resources (equal); Software (equal); Supervision (equal); Validation (equal); Visualization (equal); Writing – original draft (equal); Writing – review & editing (equal).

DATA AVAILABILITY

The data that support the findings of this study are available from the author upon reasonable request.

APPENDIX A: COMPUTATION OF WEISSENBERG NUMBER

In this work, the Weissenberg number is defined in a consistent manner with the typical treatment done in the literature for Maxwellian fluids, as follows:

$$\mathrm{Wi}(\tilde{\omega}) \equiv 2t_r\left(-\frac{W_I^2}{8\mu}\left(\frac{\partial p}{\partial z}\right)_0\right)\left(\frac{1}{H_I}\right) \times \frac{1}{N}\sum_{j=2,even}^{2N}\frac{1}{\tilde{x}_{fin,j}-\tilde{x}_{ini,j}}\left|\int_{\tilde{x}_{ini,j}}^{\tilde{x}_{fin,j}}\frac{\partial \hat{v}_{II,j}}{\partial \tilde{y}}\left(\tilde{x},\tilde{y}=\frac{1}{2f},\tilde{\omega}\right)d\tilde{x}\right|. \tag{A1}$$

APPENDIX B: GITHUB LINK TO CODE SOURCE

The code developed to summarize the methodology employed in this work is available under an open source license on GitHub at the following URL: https://www.github.com/utorresh/anomalous_ slip_maxwell

REFERENCES

Alastruey, J., Xiao, N., Fok, H., Schaeffter, T., and Figueroa, C. A., "On the impact of modelling assumptions in multi-scale, subject-specific models of aortic haemodynamics," J. R. Soc. Interface **13**, 20160073 (2016).

Alexeev, D., Amoudruz, L., Litvinov, S., and Koumoutsakos, P., "Mirheo: High-performance mesoscale simulations for microfluidics," Comput. Phys. Commun. **254**, 107298 (2020).

Bolaños, S. J. and Vernescu, B., "Derivation of the Navier slip and slip length for viscous flows over a rough boundary," Phys. Fluids **29**, 057103 (2017).

Borg, M. K., Lockerby, D. A., and Reese, J. M., "A hybrid molecular-continuum simulation method for incompressible flows in micro/nanofluidic networks," Microfluid. Nanofluid. **15**, 541–557 (2013).

Chashechkin, Y. D., "Differential fluid mechanics—harmonization of analytical, numerical and laboratory models of flows," *Mathematical Modeling and Optimization of Complex Structures* (Springer, Cham, 2016), pp. 61–91.

Collepardo-Guevara, R. and Corvera Poiré, E., "Controlling viscoelastic flow by tuning frequency during occlusions," Phys. Rev. E **76**, 026301 (2007).

Corral-Casas, C., Chen, Y., Borg, M. K., and Gibelli, L., "Density and confinement effects on fluid velocity slip," Phys. Rev. Fluids **9**, 034201 (2024).

Corvera Poiré, E. and Hernández-Machado, A., "Frequency-induced stratification in viscoelastic microfluidics," Langmuir **26**, 15084–15086 (2010).

Dou, J., Yang, Z., Singh, B., Ma, B., Lu, Z. *et al.*, "Discussion: Embracing microfluidics to advance environmental science and technology," Sci. Total Environ. **937**, 173597 (2024).

Flores Gerónimo, J., Hernández-Machado, A., and Corvera Poiré, E., "Contact line dynamics of pulsatile fluid interfaces modulated by patterned substrates," Phys. Fluids **34**, 052001 (2022).

Hagsäter, S. M., Jensen, T. G., Bruus, H., and Kutter, J. P., "Acoustic resonances in microfluidic chips: Full-image micro-PIV experiments and numerical simulations," Lab Chip **7**, 1336–1344 (2007).

Islam, M. A., Hossain, A., Hossain, N., Ahmed, M. M. S., Islam, S. *et al.*, "Recent achievement of graphene in biomedicine: Advancements by integrated microfluidics system and conventional techniques," Sens. Int. **5**, 100293 (2024).

Jin, Q. and Ren, Y., "Review on mechanics of fluid-conveying nanotubes," Int. J. Eng. Sci. **195**, 104007 (2024).

Kapoor, K., Amandeep, and S., Patil., "Viscoelasticity and shear thinning of nanoconfined water," Phys. Rev. E **89**, 013004 (2014).

Kenari, M. A., Rezvani Ghomi, E., Akbari Kenari, A., Arabi, S. M. S., Deylami, J. *et al.*, "Biomedical applications of microfluidic devices: Achievements and challenges," Polym. Adv. Technol. **33**, 3920–3934 (2022).

Liu, R., Jiang, Y., Li, B., and Wang, X., "A fractal model for characterizing fluid flow in fractured rock masses based on randomly distributed rock fracture networks," Comput. Geotech. **65**, 45–55 (2015).

Liu, R., Li, B., and Jiang, Y., "A fractal model based on a new governing equation of fluid flow in fractures for characterizing hydraulic properties of rock fracture networks," Comput. Geotech. **75**, 57–68 (2016).

Mohamed, K. M. and Mohamad, A., "A review of the development of hybrid atomistic–continuum methods for dense fluids," Microfluid. Nanofluid. **8**, 283–302 (2010).

Neužil, P., Giselbrecht, S., Länge, K., Huang, T. J., and Manz, A., "Revisiting lab-on-a-chip technology for drug discovery," Nat. Rev. Drug Discovery **11**, 620–632 (2012).

Ochoa, A., Gastélum, G., Rocha, J., and Olguin, L. F., "High-throughput bacterial co-encapsulation in microfluidic gel beads for discovery of antibiotic-producing strains," Analyst **148**, 5762–5774 (2023).

Öttinger, H. C. and Venerus, D. C., "Thermodynamic approach to interfacial transport phenomena: Single-component systems," AIChE J. **60**, 1424–1433 (2014).

Priest, C., "Surface patterning of bonded microfluidic channels," Biomicrofluidics **4**, 032206 (2010).

Sagis, L. M. and Öttinger, H. C., "Dynamics of multiphase systems with complex microstructure. I. Development of the governing equations through nonequilibrium thermodynamics," Phys. Rev. E **88**, 022149 (2013).

Shang, L., Cheng, Y., and Zhao, Y., "Emerging droplet microfluidics," Chem. Rev. **117**, 7964–8040 (2017).

Si, Y., Li, C., Hu, J., Zhang, C., and Dong, Z., "Bioinspired superwetting open microfluidics: From concepts, phenomena to applications," Adv. Funct. Mater. **33**, 2301017 (2023).

Soltani, M. and Chen, P., "Numerical modeling of interstitial fluid flow coupled with blood flow through a remodeled solid tumor microvascular network," PLoS One **8**, e67025 (2013).

Squires, T. M. and Quake, S. R., "Microfluidics: Fluid physics at the nanoliter scale," Rev. Mod. Phys. **77**, 977–1026 (2005).

Stoecklein, D. and Di Carlo, D., "Nonlinear microfluidics," Anal. Chem. **91**, 296–314 (2019).

Thomas, J. A. and McGaughey, A. J., "Water flow in carbon nanotubes: Transition to subcontinuum transport," Phys. Rev. Lett. **102**, 184502 (2009).

Thompson, R. L. and Oishi, C. M., "Reynolds and Weissenberg numbers in viscoelastic flows," J. Non-Newtonian Fluid Mech. **292**, 104550 (2021).

Tomita, M., Hirose, S., Nakamura, T., and Funamoto, K., "pH-dependent migratory behaviors of neutrophil-like cells in a microfluidic device with controllability of dissolved gas concentrations," Sci. Rep. **14**, 28730 (2024).

Torres-Herrera, U., "Dynamic permeability of fluids in rectangular and square microchannels: Shift and coupling of viscoelastic bidimensional resonances," Phys. Fluids **33**, 012016 (2021).

Torres-Herrera, U., "Analytical study of symmetry breaking and frequency mixing effects in the oscillatory dynamics of fluids within bent nanotubes," Microfluid. Nanofluid. **26**, 13 (2022).

Torres-Herrera, U. and Corvera Poiré, E., "A continuum model to study fluid dynamics within oscillating elastic nanotubes," J. Fluid Mech. **916**, A16 (2021).

Torres-Herrera, U. and Nakamura, K., "Flow differentiation within nanotube networks with symmetric bifurcations by local bending vibration: A theoretical study," J. Fluids Struct. **109**, 103502 (2022).

Turkyilmazoglu, M., "Single phase nanofluids in fluid mechanics and their hydrodynamic linear stability analysis," Comput. Methods Programs Biomed. **187**, 105171 (2020).

Vazquez-Vergara, P., Torres-Herrera, U., Caballero-Robledo, G. A., Olguin, L. F., and Corvera Poiré, E., "Experimental resonances in viscoelastic microfluidics," Front. Phys. **9**, 636070 (2021a).

Vazquez-Vergara, P., Torres-Herrera, U., Olguin, L. F., and Corvera Poiré, E., "Singular behavior of microfluidic pulsatile flow due to dynamic curving of air-fluid interfaces," Phys. Rev. Fluids **6**, 024003 (2021b).

Weinan, E., *Principles of Multiscale Modeling* (Cambridge University Press, 2011).

Yuan, C., Zhang, H.-N., Li, Y.-K., Li, X.-B., Wu, J. *et al.*, "Nonlinear effects of viscoelastic fluid flows and applications in microfluidics: A review," Proc. Inst. Mech. Eng., Part C **234**, 4390–4414 (2020).

Zampogna, G. A., Magnaudet, J., and Bottaro, A., "Generalized slip condition over rough surfaces," J. Fluid Mech. **858**, 407–436 (2019).